Quantum transport properties of single-crystalline Ag$_2$Se$_{0.5}$Te$_{0.5}$ nanowires as a new topological material†

Minjin Kim,[a] Jihwan Kim,[b] In-Ho Lee,[b] Woo Hyun Han, [iD][c] Yun Chang Park,[d] Woo Youn Kim, [iD] *[a] Bongsoo Kim [iD] *[a] and Junho Suh [iD] *[b]

We report a ternary silver chalcogenide, Ag$_2$Se$_{0.5}$Te$_{0.5}$, as a new topological material with improved quantum transport properties. Single-crystalline nanostructures of ternary silver chalcogenides Ag$_2$Se$_x$Te$_{1−x}$ are synthesized with a tunable chemical composition *via* the chemical vapor transport method. Quantum transport studies reveal that Ag$_2$Se$_{0.5}$Te$_{0.5}$ nanowires present topological surface states with higher electron mobility and longer mean free path compared to binary Ag-chalcogenides. First-principles calculations also indicate that Ag$_2$Se$_{0.5}$Te$_{0.5}$ is a topological insulator, and the observed enhancement in transport properties could imply reduced bulk carrier contribution in the new ternary silver chalcogenide.

Introduction

Topological insulators[1,2] and Weyl[3–5] and Dirac semimetals[6–8] are novel quantum materials with nontrivial topological surface states. They have been recognized as promising platforms for future spintronic applications and fundamental physics research,[9–11] and investigations into new topological materials are being actively conducted in condensed matter physics and materials science. In addition, efforts to improve material performance and tune the topological properties have been pursued *via* electrostatic gating,[12–14] material doping,[14–16] and chemical component engineering.[17–24]

Among such approaches, the chemical component engineering technique enhances material performance by controlling chemical potential[16,21] or by reducing defect formation.[17–19] It even makes it possible to manipulate the Weyl and Dirac carrier properties by tuning the crystal structure and modifying the band structure of the topological surface states.[20–24] The benefits of chemical component engineering have been demonstrated with bismuth-based compounds such as Bi$_x$Sb$_{1−x}$, Bi$_2$Se$_3$, and Bi$_2$Te$_3$, which are topological insulators with isotropic Dirac cones,[18–21] transition metal pnictide compounds such as NbP, TaP, and TaAs, which are topological Weyl semimetals,[22] and also Heusler compounds.[23,24]

In recent studies, binary silver-based chalcogenides have been identified as topological materials with nontrivial topological surface states and inverted band structures by strong spin–orbit coupling.[25–31] Ag$_2$Se has been predicted to be a topological semimetal with an anisotropic Fermi pocket,[25–27] and Ag$_2$Te has been reported as a topological insulator with an anisotropic Dirac cone,[28–31] which could be an excellent spin conductor with one-directional spin transport[32] and a long spin-relaxation time.[33] Here, we study a ternary Ag-chalcogenide, Ag$_2$Se$_{0.5}$Te$_{0.5}$, to demonstrate that chemical component engineering can be applied to Ag-based topological materials, exhibiting a transition from a topological semimetal to a topological insulator.

We synthesize single-crystalline ternary Ag$_2$Se$_x$Te$_{1−x}$ nanostructures with tunable chemical compositions using the chemical vapor transport (CVT) method. First-principles calculations indicate that the ternary compounds undergo a transition from a topological semimetal (Ag$_2$Se) to a topological insulator (Ag$_2$Te). The calculations also suggest that Ag$_2$Se$_{0.5}$Te$_{0.5}$ can be a new ternary topological insulator with nontrivial topological surface states, which is also evidenced by measurements of the electron transport properties of Ag$_2$Se$_{0.5}$Te$_{0.5}$ nanowires (NWs). We observe quantum interference effects, such as the Aharonov–Bohm (AB) oscillation and weak anti-localization (WAL), induced by the helical electron transport along the surface of the NW. The Shubnikov–de Haas (SdH) oscillation is also observed, with a Berry phase of π indicating that the conductance oscillation originates from the

[a] Department of Chemistry, KAIST, 291 Daehak-ro, Yuseong-gu, Daejeon 34141, Korea. E-mail: wooyoun@kaist.ac.kr, comnsi@gmail.com
[b] Korea Research Institute of Standards and Science (KRISS), 267 Gajeong-ro, Yuseong-gu, Daejeon 34113, Korea. E-mail: junho.suh@kriss.re.kr
[c] Department of Physics, KAIST, 291 Daehak-ro, Yuseong-gu, Daejeon 34141, Korea
[d] Department of Measurement and Analysis, National NanoFab Center, 291 Daehak-ro, Yuseong-gu, Daejeon 34141, Korea
† Electronic supplementary information (ESI) available. See DOI: 10.1039/c9nr00288j

nontrivial topological surface states. Ultimately, from the SdH oscillation, we obtain higher electron mobility and longer elastic mean free path compared to those of Ag_2Se and Ag_2Te. Such enhancement in electronic transport properties could originate from reduced defect formation[17–19] and suppressed bulk carrier contribution due to the modified band structure.

Results and discussion

Ternary Ag-chalcogenide nanostructures with a tunable chemical composition

Single-crystalline ternary $Ag_2Se_xTe_{1-x}$ nanostructures with a tunable composition are grown *via* the CVT method using a mixture of Ag_2Se and Ag_2Te powders as a precursor (Fig. S1†). At a reaction temperature of 1000–1050 °C, $Ag_2Se_xTe_{1-x}$ nanostructures are synthesized with clean surfaces and well-defined facets, as shown in the scanning electron microscopy (SEM) images in Fig. 1a and b. The NWs are a few tens of micrometers long and have hexagonal cross-sections (Fig. 1d) with diameters of 70–200 nm, and the nanoplates have widths of 3–5 μm and lengths of 5–10 μm. The selenium composition x in $Ag_2Se_xTe_{1-x}$ nanostructures is controlled by adjusting the molar ratio of the precursor, as indicated in Fig. 1c, and the three elements Ag, Se, and Te are distributed homogeneously in the synthesized nanostructures for the whole range of x, as shown in energy-dispersive X-ray spectroscopy (EDS) images (inset in Fig. 1c and Fig. S2†).

We perform structural and compositional analyses of the $Ag_2Se_xTe_{1-x}$ NWs with $x = 0.5$ (*i.e.* $Ag_2Se_{0.5}Te_{0.5}$) in detail using X-ray diffraction (XRD) and transmission electron microscopy (TEM). From the XRD pattern (Fig. S3†) and TEM analysis (Fig. S4†) of the as-synthesized $Ag_2Se_{0.5}Te_{0.5}$, we confirm that it has a single-phase orthorhombic crystal structure with lattice parameters of $a = 4.43$ Å, $b = 7.23$ Å, and $c = 7.97$ Å.[34] A cross-sectional TEM image of the $Ag_2Se_{0.5}Te_{0.5}$ NW is shown in Fig. 1d, and the corresponding selected area electron diffraction (SAED) patterns (Fig. 1e) present clear spots, verifying that the NW is single-crystalline. Further TEM and EDS analyses (Fig. S4†) reveal that all of the synthesized $Ag_2Se_{0.5}Te_{0.5}$ nanostructures are single-crystalline with an elemental composition of Ag : Se : Te = 2 : 0.5 : 0.5. The [100] zone axis of the SAED patterns (Fig. 1e) corresponds to the NW growth direction (Fig. S4†), and a high-resolution TEM image (Fig. 1f) and fast Fourier transform (FFT) pattern (inset in Fig. 1f) indicate that the $Ag_2Se_{0.5}Te_{0.5}$ NW is in a single-crystalline orthorhombic phase. The lattice spacings of 7.23 Å and 7.96 Å in the high-resolution TEM images (Fig. 1f) match well with those of the (010) and (001) atomic planes of an orthorhombic $Ag_2Se_{0.5}Te_{0.5}$ crystal structure.

Previous studies suggest that ternary $Ag_2Se_{0.5}Te_{0.5}$ could have three distinct features. First, ternary compounds have a more stable, ordered structure with higher impurity formation energy than binary compounds, which suppresses defect formation.[17–19] Second, alloying Ag_2Se with Te shifts the Fermi level toward the Dirac point by moving the n-type pinning
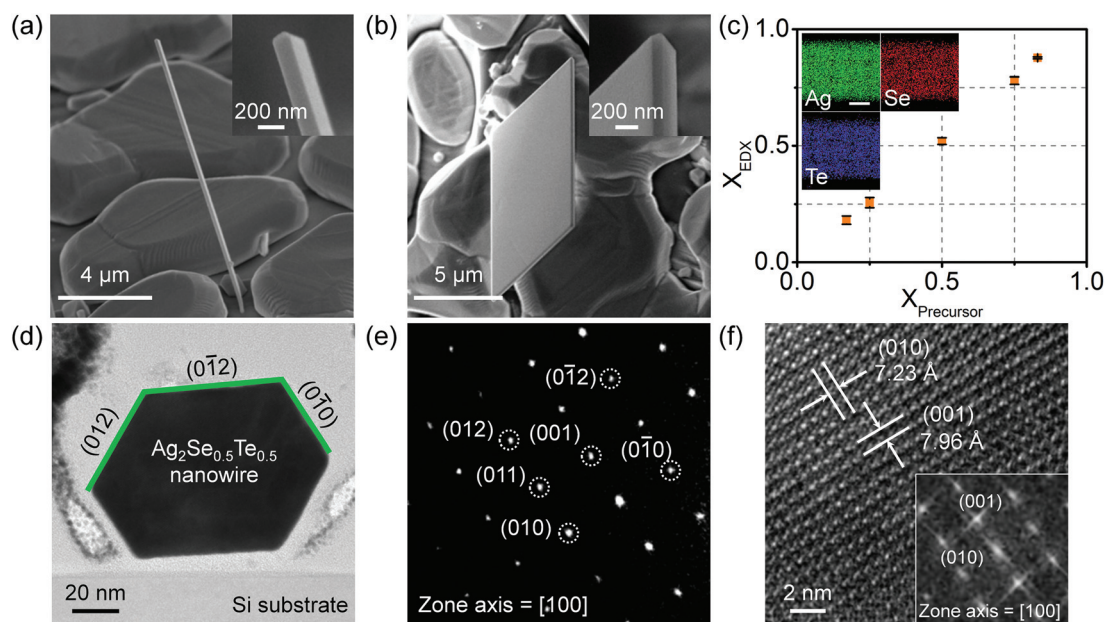

Fig. 1 Analysis of the synthesized single-crystalline $Ag_2Se_xTe_{1-x}$ nanostructure. (a, b) SEM images of the (a) $Ag_2Se_xTe_{1-x}$ NW and (b) $Ag_2Se_xTe_{1-x}$ nanoplate, synthesized with Ag_2Se and Ag_2Te powders at a 1 : 1 molar ratio. Insets in (a) and (b) are enlarged SEM images showing well-defined facets at the tips and sides. (c) Composition x in $Ag_2Se_xTe_{1-x}$ NWs *versus* mole fraction of Ag_2Se powder in the precursor, $X_{precursor} = Ag_2Se/(Ag_2Se + Ag_2Te)$. (Insets) Representative EDS elemental mapping images showing homogeneous atomic distribution of Ag, Se, and Te ($X_{precursor} = 0.5$). Scale bar, 50 nm. (d) Cross-sectional TEM image of the $Ag_2Se_{0.5}Te_{0.5}$ NW. (e) SAED pattern of the $Ag_2Se_{0.5}Te_{0.5}$ NW along the [100] zone axis. (f) High-resolution TEM image of (d) and (inset) FFT pattern, indicating that the $Ag_2Se_{0.5}Te_{0.5}$ NW has a single-crystalline orthorhombic structure.

energy toward the conduction band minimum.[35] Third, incorporating two different Ag_2Se and Ag_2Te compounds leads to a change in the lattice parameters and varies the crystal structure due to the different Se and Te atomic sizes, thereby modifying the band structure and changing the topological properties.[34,36]

Topological electronic structure of $Ag_2Se_{0.5}Te_{0.5}$ NWs

Previous reports have indicated that the band structure of Ag_2Se shows characteristics of a topological semimetal with a band overlap,[25–27] while the band structure of Ag_2Te shows characteristics of a topological insulator with a single Dirac point in the band gap and an anisotropic Dirac cone.[28–31] As the composition changes from Ag_2Se to Ag_2Te, crystal structure and energy band structure modifications are expected in the resulting ternary alloy compounds, e.g., $Ag_2Se_{0.5}Te_{0.5}$. However, both the formation procedure of the specific crystal structure and the corresponding nontrivial topological nature in the electronic structure are not known yet.

To clarify the topological properties and band structure of ternary $Ag_2Se_{0.5}Te_{0.5}$, we perform first-principles calculations based on density functional theory. After an exhaustive investigation using an *ab initio* crystal structure searching protocol,[37] we found an orthorhombic crystal structure ($Pmn2_1$, space group number 31) with lattice parameters of $a = 4.50$ Å, $b = 7.23$ Å, and $c = 7.97$ Å, which is consistent with the experimentally determined crystal structure. The schematics of the crystal structure are shown in Fig. S5† and the corresponding atomic coordinates are listed in Table S1,† respectively. The calculated total energy relative to the crystal with the lowest total energy is 19 meV per atom. From the band structure calculation (Fig. 2), $Ag_2Se_{0.5}Te_{0.5}$ is determined to be a non-layered ternary compound showing band inversion between s and p orbitals at the high symmetry point, and a clear signature of the topological insulator develops as the spin–orbit coupling is included. Fig. 2a shows the bulk band struc-

ture with an opened band gap, and Fig. 2b shows the surface band structure with topological states. The bulk band gap is around 40 meV. Without spin–orbit coupling, the gap is closed.

Z_2 topological invariants similar to the genus in topology classify the topological properties of time-reversal invariant systems. By calculating the Wilson loop,[38] we acquire the topological index as $Z_2 = (1;0,0,0)$ of ternary compounds with no inversion symmetry, which demonstrates that $Ag_2Se_{0.5}Te_{0.5}$ is a strong topological insulator. We conduct further band structure calculations by changing the crystal lattice parameter a and find the modulation of the topological properties: the calculated band structures show topological semimetal characteristics when the lattice parameter a is smaller than 4.40 Å, and trivial insulator characteristics when the lattice parameter a is larger than 4.70 Å. As the chemical composition changes from Ag_2Se to Ag_2Te, we observe band structure modification and topological property transition with a reduced bulk contribution in the ternary compound $Ag_2Se_{0.5}Te_{0.5}$. Our calculations of band inversion and topological invariants reveal the topological nature of $Ag_2Se_{0.5}Te_{0.5}$ and suggest the ternary silver chalcogenide as a new ternary topological insulator with anisotropy.

Aharonov–Bohm oscillation in $Ag_2Se_{0.5}Te_{0.5}$ NWs

We perform low-temperature transport measurements to demonstrate the quantum electronic properties of $Ag_2Se_{0.5}Te_{0.5}$ NWs. The device scheme and the corresponding SEM image are shown in Fig. 3a and b; detailed device fabrication procedures and measurement techniques are described in the Experimental section. By applying a magnetic field (B) parallel to the NW axis ($\theta = 0°$), magneto-conductance G is measured at 2 K with device 1. Fig. 3c plots the observed magneto-conductance change (ΔG) after subtraction of the smooth background, which shows a pronounced periodic oscillation with a period of $\Delta B = 0.80$ T (indicated by the vertical dashed lines). The major peak in the FFT spectrum (Fig. 3d) indicates the
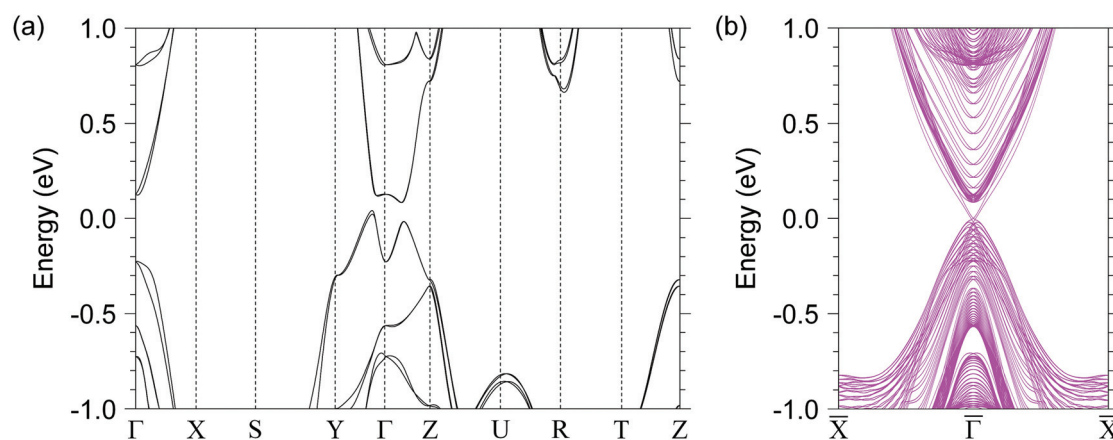

Fig. 2 Electronic band structure of $Ag_2Se_{0.5}Te_{0.5}$ with spin–orbit coupling. (a) Bulk and (b) surface band structure of $Ag_2Se_{0.5}Te_{0.5}$. A typical band inversion between s and p orbitals is found. Spin–orbit coupling is required to open the gap and make a system topological insulator, suggesting the existence of topological surface states in the $Ag_2Se_{0.5}Te_{0.5}$ system.
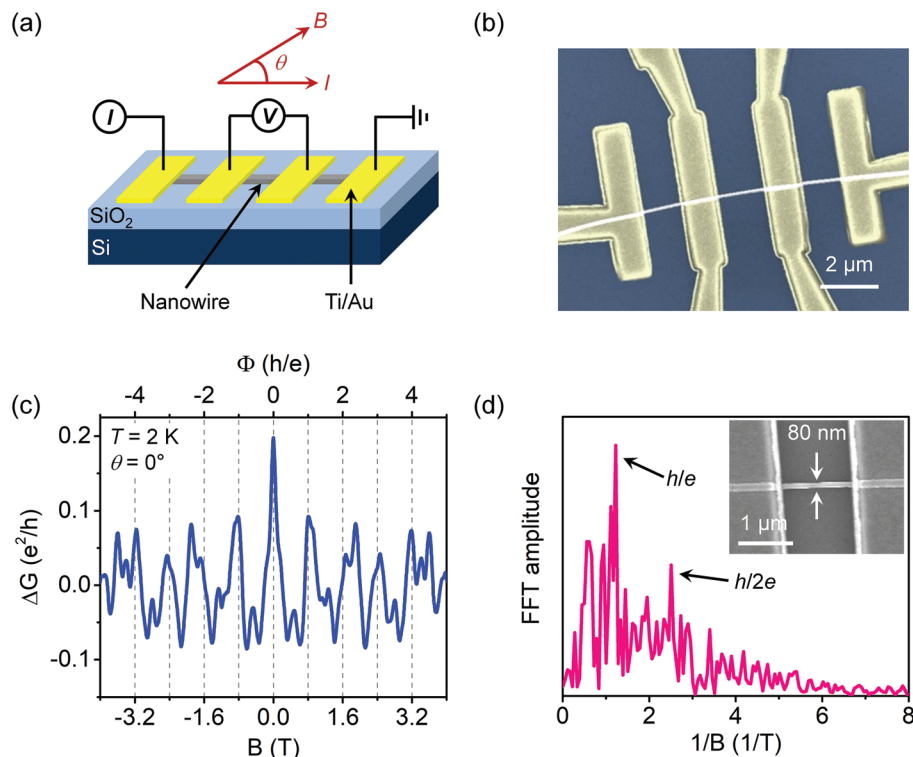
Fig. 3 Magneto-conductance oscillations in the $Ag_2Se_{0.5}Te_{0.5}$ NW. (a) Schematic of the four-probe measurement configuration (θ : angle between magnetic field and current). (b) SEM image of a fabricated device. (c) ΔG *versus* B showing oscillation with an h/e period of $\Delta B = 0.80$ T from device 1 at $T = 2$ K. The magnetic field direction is parallel to the NW axis ($\theta = 0°$). (d) FFT spectrum of ΔG in (c). The arrows indicate the peak positions of $1/B = 1.25$ T^{-1} for the h/e period and $1/B = 2.50$ T^{-1} for the $h/2e$ period. (Inset) SEM image of device 1 showing NW dimensions: thickness (t) = 70 nm and width (w) = 80 nm.

same oscillation period. Such a periodic oscillation in magneto-conductance is due to the AB oscillation,[39] which indicates helical electron transport along the surface of the $Ag_2Se_{0.5}Te_{0.5}$ NW.

In topological insulator NWs, surface carriers travel the perimeter of the NW while maintaining their phase coherence. When an external magnetic field is applied along the length of the NW, parallel to the direction of the electric current, electron interference results in conductance oscillation, called the AB oscillation.[12,40] The oscillation period is $\Delta B = \Phi_0/S$, where $\Phi_0 = h/e$ is the flux quantum with Planck's constant h and electron charge e, and S is the cross-sectional area of the NW. In the present work, $S = 5.60 \times 10^{-15}$ m^2 (inset in Fig. 3d) and the corresponding h/e period is $\Delta B = 0.74$ T, which is close to the observed period of $\Delta B = 0.80$ T. In Fig. 3c, there is also weak oscillation with a period of $\Delta B = 0.40$ T, as indicated by the second peak in the FFT analysis (Fig. 3d). This minor $h/2e$ period oscillation arises from the Altshuler–Aronov–Spivak (AAS) effect, which is observed in cylindrical conductors due to the interference created by carriers propagating in complete circles in opposite directions.[39,41] Theory predicts that both h/e and $h/2e$ period oscillations can be observed in topological insulator NWs.[42–44] We confirm the surface states in the $Ag_2Se_{0.5}Te_{0.5}$ NWs by observing that the AB oscillations in other NW devices with different cross-sectional areas also

show different h/e oscillation periods close to $\Delta B = \Phi_0/S$ (Fig. S6†).

In the clean limit with surface electrons, the AB oscillation peak-to-peak amplitude is expected to equal e^2/h.[14] Due to non-ideal effects in the observation of surface states, such as defects and bulk contribution, the amplitude is reduced in general.[39,45] Without gate tuning, our $Ag_2Se_{0.5}Te_{0.5}$ NW device (Fig. 3c) shows an AB oscillation peak-to-peak amplitude of $\sim 0.14e^2/h$, which is about 0.85% of total conductance ($16.7e^2/h$), whereas previously reported Ag_2Se[26] and Ag_2Te NWs[29] showed the peak-to-peak amplitudes about 0.1% of total conductance. This suggests a reduced defect formation and enhanced surface contribution in ternary component NWs. Our four different $Ag_2Se_{0.5}Te_{0.5}$ NW devices (Fig. 3c and Fig. S6†) show AB oscillation peak-to-peak amplitudes of about $0.53 \pm 0.36\%$ of total conductance. The large standard deviation implies that more refined control is still required in material engineering.

The h/e period oscillation is indeed closely related to the 1D band formation of surface electrons. According to the 1D subband model of surface states in topological insulator NWs,[14,39,45] conductance should exhibit a minimum at integer flux quanta and a maximum at half-integer flux quanta when the Fermi level is at the Dirac point. The phase of the conductance oscillation alternates as the Fermi level departs from the

Dirac point with a period of $\Delta_{1D} = h v_F / 2(w + t)$, where v_F is the Fermi velocity, and w and t are the NW width and thickness.[39] Our result in Fig. 3c shows a conductance maximum at integer flux quanta, indicating phase alternation of the conductance oscillation. Another result in Fig. S6a† with a different NW device, which is expected to have a different Fermi level, shows a conductance minimum at integer flux quanta.

Weak anti-localization effect in Ag$_2$Se$_{0.5}$Te$_{0.5}$ NWs

In addition to the AB oscillation, WAL is the quantum interference effect observed in topological insulator NWs arising from strong spin–orbit coupling and helical surface states.[18] We measure the WAL effect from the surface channels of the Ag$_2$Se$_{0.5}$Te$_{0.5}$ NW by changing the magnetic field direction axis θ (Fig. 4a) and temperature T (Fig. 4b) with device 2. Fig. 4a shows angle-dependent magneto-conductance G at $T = 2$ K. The cusp at zero magnetic field is a feature of WAL, and it becomes sharper as θ increases. We expect that the spin–orbit coupling of both surface and bulk states contributes to WAL, with the former depending only on the perpendicular component of the magnetic field.[46] To extract this surface state contribution to WAL, G measured at $\theta = 90°$ is subtracted by G measured at $\theta = 0°$.

Fig. 4c plots $\delta G = G(\theta = 90°) - G(\theta = 0°)$ at four different temperatures: $T = 2, 5, 7,$ and 10 K. The solid lines in Fig. 4c are the fit results with quasi-1D localization theory including

electron–electron interactions and spin–orbit interactions,[47] which are given by

$$\delta G = \frac{\sqrt{2} e^2}{\pi \hbar} \frac{L_n}{L} \left[\frac{3}{2} \frac{A_i \left(\frac{2L_n^2}{L_1^2} \right)}{A_i' \left(\frac{2L_n^2}{L_1^2} \right)} - \frac{1}{2} \frac{A_i \left(\frac{2L_n^2}{L_2^2} \right)}{A_i' \left(\frac{2L_n^2}{L_2^2} \right)} \right] \tag{1}$$

where $\hbar$ is the reduced Planck's constant, L is the NW channel length, L_n is the Nyquist scattering length, A_i is the Airy function, and A_i' is its derivative. Here, $L_1 = (4/3L_{so}^2 + 1/L_\varphi^2 + (ewB)^2/3\hbar^2)^{-1/2}$ and $L_2 = (1/L_\varphi^2 + (ewB)^2/3\hbar^2)^{-1/2}$, where w is the NW width, L_{so} is the spin–orbit scattering length, and L_φ is the phase coherence length. For NW dimensions of $L = 1$ μm and $w = 85$ nm, fitting δG data at $T = 2$ K to eqn (1) results in characteristic lengths of $L_\varphi = 314$ nm, $L_n = 200$ nm, and $L_{so} = 180$ nm, which are comparable to the previously reported values in Ag$_2$Se NWs.[26] The L_{so} values, which are related to spin–orbit coupling strength, from Ag$_2$Se$_{0.5}$Te$_{0.5}$ and Ag$_2$Se NWs[26] are approximately five times larger than those from Bi$_2$Se$_3$ nanoribbons[47] and Bi$_2$Te$_3$ NWs.[46] The obtained characteristic lengths at other temperatures are plotted in Fig. 4d, where solid lines show power-law dependence on temperature, making L_φ, L_n, and L_{so} behave as $T^{-0.29}$, $T^{-0.28}$, and $T^{-0.23}$, respectively. As the temperature increases, the WAL effect disappears (Fig. 4b) and all characteristic lengths decrease (Fig. 4d) due to an increase in thermal scattering.[26] It is known that L_φ and L_n are proportional to $T^{-1/3}$ in 1D systems
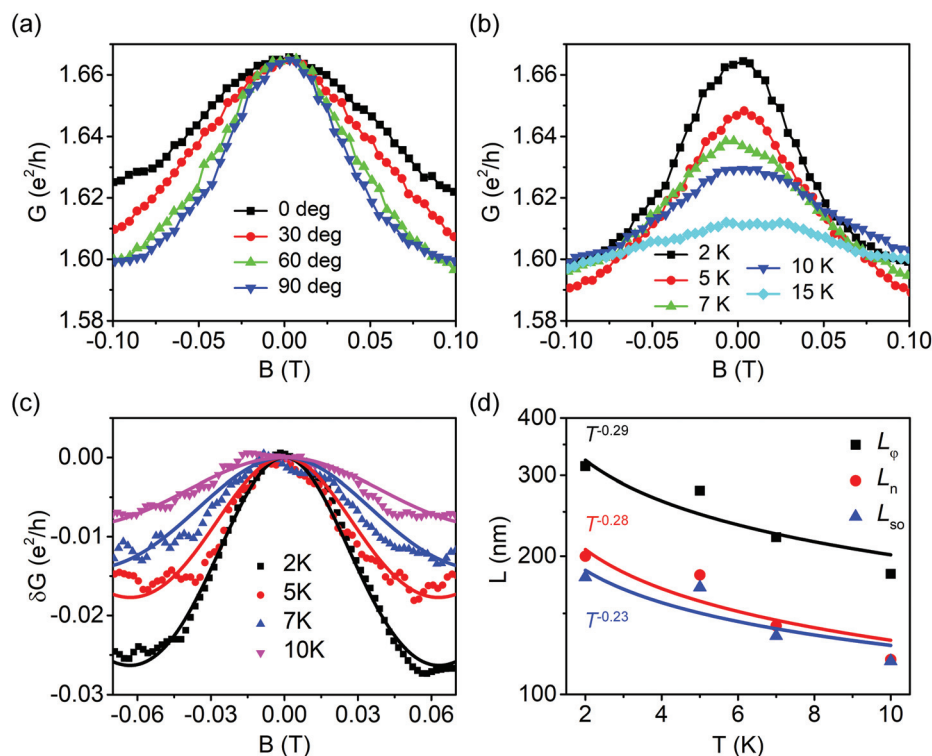

Fig. 4 WAL effects in the Ag$_2$Se$_{0.5}$Te$_{0.5}$ NW from device 2. (a) Angle dependence of magneto-conductance at $T = 2$ K. (b) Temperature dependence of magneto-conductance at $\theta = 90°$. (c) Temperature dependence of $\delta G = G(\theta = 90°) - G(\theta = 0°)$, which indicates the surface contribution to WAL. Solid lines are the fit results with quasi-1D localization theory. (d) Temperature dependence of characteristic lengths L_φ, L_n, and L_{so}, with power-law fits (solid lines).

and $T^{-1/2}$ in 2D systems;[46,47] exponents obtained from the temperature dependence of L_φ and L_n in Fig. 4d indicate that electron transport in $Ag_2Se_{0.5}Te_{0.5}$ NWs is close to 1D.

Shubnikov–de Haas oscillation in $Ag_2Se_{0.5}Te_{0.5}$ NWs

We also observe the SdH oscillation originating from the topological surface states in the $Ag_2Se_{0.5}Te_{0.5}$ NW. We apply magnetic field B perpendicular to the NW axis ($\theta = 90°$), and measure magneto-resistances R with device 3 at 2 K, as shown in the inset of Fig. 5a. After subtracting the smooth background, magneto-resistance change (ΔR) curves are plotted as a function of $1/B$ in Fig. 5a. ΔR oscillates periodically at $1/B$, indicating the SdH oscillation, the period of which (B_F) is extracted by FFT analysis (inset of Fig. 5b). The pronounced peak in the FFT spectrum indicates $B_F = 44.1$ T. The solid line in the ΔR vs. $1/B$ graph (Fig. 5a) is a fit to the Lifshitz–Kosevich (LK) theory,[31,48]

$$\Delta R = A \exp\left(-\frac{\pi}{\mu B}\right) \cos\left[2\pi\left(\frac{B_F}{B} + \frac{1}{2} + \gamma\right)\right] \quad (2)$$

where μ is the carrier mobility, $2\pi\gamma$ is the Berry phase, and A is a temperature-dependent parameter discussed in the next paragraph. Because Dirac fermions carry a Berry phase of π, phase factor γ is expected to be 0 for topological trivial elec-

trons and 0.5 for Dirac fermions. From the fit results, we obtain $\gamma = 0.4$, supporting the existence of a π Berry phase due to topological surface states. The LK fitting results in a SdH oscillation period B_F of 44.5 T, which is close to the FFT result, and an electron mobility μ of 2300 cm^2 s^{-1} V^{-1}. B_F is determined from the cross-sectional Fermi surface area S_F by the relation of $1/B_F = 2\pi e/\hbar S_F$, where $S_F = \pi k_F^2$ and k_F is the Fermi wave vector. The 2D carrier concentration at the surface n_{2D} is related to k_F by $k_F^2/4\pi$. With $B_F = 44.5$ T, k_F and n_{2D} are estimated to be 0.368 nm^{-1} and 1.08×10^{12} cm^{-2}, respectively. Then, the elastic mean free path $l_e = \hbar\mu k_F/e$ is calculated to be 55.6 nm. We list the parameters from the LK theory fit in Table S2.† We note that the elastic mean free path l_e of $Ag_2Se_{0.5}Te_{0.5}$ NWs is longer than that of Ag_2Se NWs, which is about $l_e \sim 20$ nm.[26] Also, the electron mobility μ of $Ag_2Se_{0.5}Te_{0.5}$ NWs obtained from the SdH oscillation is relatively higher than that of Ag_2Se ($\sim$580 cm^2 s^{-1} V^{-1}) and Ag_2Te ($\sim$1310 cm^2 s^{-1} V^{-1}).[26,31] As the mean free path and surface carrier mobility are affected by defects and scattering,[49] the longer mean free path and higher mobility signal that alloying Ag_2Se with Te might decrease defects and reduce conduction band carriers.[13] Finally, Fig. 5b shows a Landau-level fan diagram, which is a plot of the ΔR maxima and minima positions as a function of Landau-level numbers (see ESI Fig. S7†). The slope of the straight line in the fan diagram gives the
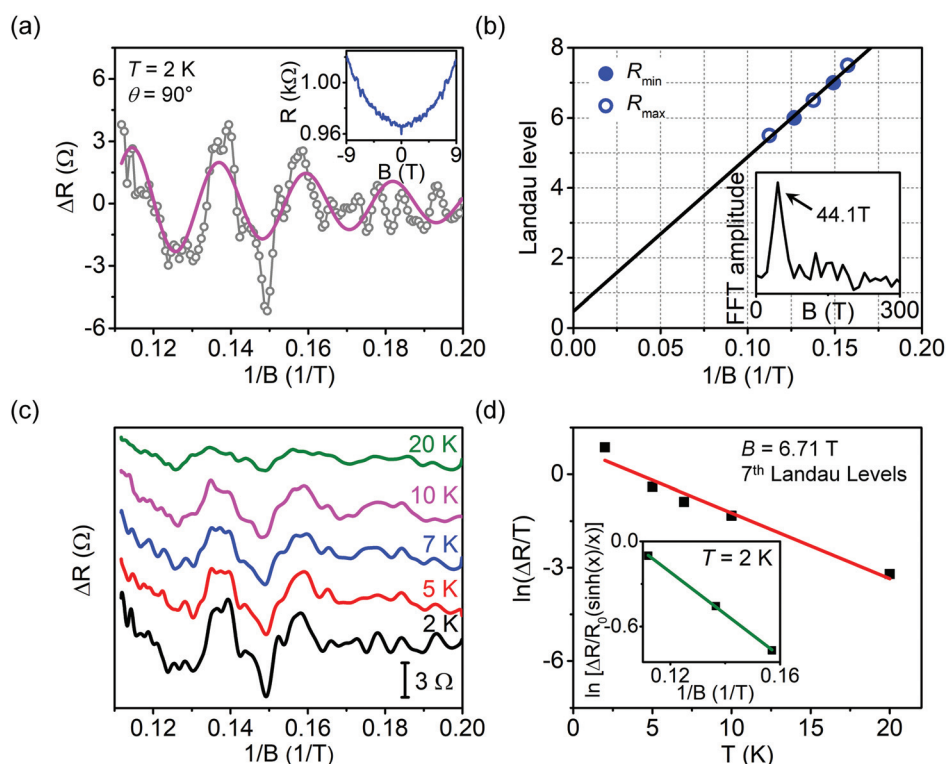

Fig. 5 The SdH oscillation in the $Ag_2Se_{0.5}Te_{0.5}$ NW from device 3. (a) ΔR curve oscillating periodically at $1/B$ at $T = 2$ K when B is perpendicular to the NW axis ($\theta = 90°$). The solid line is a fit to the LK theory. (Inset) R versus B. (b) Landau-level index versus $1/B$. (Inset) FFT spectrum of ΔR with a peak at $B_F = 44.1$ T. (c) Temperature dependence of the SdH oscillation. (d) Temperature dependence of the SdH amplitudes measured at $B = 6.71$ T (7th Landau level). (Inset) Dingle plot $\ln[(\Delta R(T, B)/\Delta R(0, B))/(\sinh(\chi)/\chi)]$ versus $1/B$ for $T = 2$ K.

same B_F as the FFT result. The intercept of the fan diagram is a phase of oscillation γ, which at about 0.5 reveals again that the SdH oscillation originates from the topological surface states.

Now, in order to obtain the Fermi energy and Fermi velocity of the $Ag_2Se_{0.5}Te_{0.5}$ NW, we measure the temperature dependence of the SdH oscillation. Fig. 5c shows ΔR obtained from R at different temperatures. The frequency of the oscillations is mostly constant over the temperature change, but the amplitude of the oscillations decreases as the temperature increases due to the thermal fluctuation of electrons on the Landau levels.[31] The temperature-dependent parameter A in the LK theory (eqn (2)) is given by[31,48]

$$\frac{\Delta R(T,B)}{\Delta R(0,B)} \approx \frac{\chi}{\sinh(\chi)} \exp\left(-\frac{2\pi^2 k_B m^* T_D}{e\hbar B}\right) \qquad (3)$$

with $\chi = 2\pi^2 k_B m^* T/(e\hbar B)$, where m^* is the cyclotron effective mass of the electrons, and k_B is the Boltzmann constant. $T_D = \hbar/(2\pi k_B \tau)$ is the Dingle temperature, where τ is the scattering time. We rewrite eqn (3) as $\ln(\Delta R(T,B)/T) \approx C - (2\pi^2 k_B m^* T_D/(e\hbar B))T$, where C is a temperature-independent term.[48] We plot $\ln(\Delta R(T, B)/T)$ *vs.* T when $B = 6.71$ T for the 7th Landau level in Fig. 5d; from the slope of the linear fit, we obtain $m^* = 0.096$ m_e with electron mass m_e. Using the relation of $V_F = \hbar k_F/m^*$ and $E_F = m^* V_F^2/2$, the estimated Fermi velocity V_F and Fermi energy E_F are 4.42×10^5 m s^{-1} and 53.5 meV, respectively. The inset in Fig. 5d shows the Dingle plot for $T = 2$ K, which is a plot of $\ln[(\Delta R(T, B)/\Delta R(0, B))/(\sinh(\chi)/\chi)]$ *vs.* $1/B$. The slope of the plot yields a Dingle temperature of $T_D = 10.5$ K and a scattering time of $\tau = 1.16 \times 10^{-13}$ s. A mean free path ($l_e = V_F\tau$) of 51.5 nm and a mobility ($\mu = e\tau/m^*$) of 2130 cm^2 s^{-1} V^{-1} are obtained from the Dingle plot, values that are close to those from the LK theory fit in Fig. 5a. The obtained physical parameters from the temperature dependence of the SdH oscillation are listed in Table S3.†

Conclusions

In this work, we synthesize single-crystalline ternary Ag-chalcogenide $Ag_2Se_xTe_{1-x}$ nanostructures with a tunable chemical composition and study their quantum electronic properties through transport measurements. We observe quantum interference effects, namely, AB oscillations and WAL, experimentally supporting the existence of conducting surface states. We also observe the SdH oscillation with a π Berry phase, indicating that such an oscillation originates from nontrivial topological surface states. Compared to binary Ag-chalcogenides, our ternary sample achieves higher electron mobility and longer elastic mean free path, possibly as a result of its modified band structure and reduced bulk contribution, which are supported by the band calculations. *Via* chemical component engineering in Ag-based topological materials, we demonstrate that the band structure can be manipulated, thereby enabling control of the topological states and adjustment of chemical potential. With further studies on the electronic structure and

finer chemical composition tuning, we expect that ternary Ag-chalcogenides, as controllable topological materials, could find novel applications in future topological material-based spintronics with improved material performance.

Experimental section

Synthesis of $Ag_2Se_xTe_{1-x}$ nanostructures

We synthesize single-crystalline ternary $Ag_2Se_xTe_{1-x}$ nanostructures—NWs, nanoribbons, and nanoplates—in a horizontal hot-wall furnace using the CVT method (Fig. S1†). A mixture of Ag_2Se (Sigma-Aldrich) and Ag_2Te (Sigma-Aldrich) powders is placed in an alumina boat at the front of the heating zone, and non-polished sapphire (c-Al_2O_3) substrates are placed ~12 cm from the boat. After purging with carrier Ar gas (99.999%) for 30 min, the temperature is raised to 1000–1050 °C at a rate of 30 °C min^{-1} with an Ar gas supply at a rate of 30 sccm. The reaction time is 45 min and the chamber pressure is maintained at 0.5 Torr. At a reaction temperature of 1000 °C, $Ag_2Se_xTe_{1-x}$ NWs are synthesized, while all $Ag_2Se_xTe_{1-x}$ NWs, nanoribbons, and nanoplates are simultaneously synthesized by increasing the reaction temperature to 1050 °C. The chemical compositions of ternary $Ag_2Se_xTe_{1-x}$ nanostructures are controlled by adjusting the amounts of Ag_2Se powder and Ag_2Te powder. Except for the reaction temperature and the composition of the mixture, all other reaction conditions including the reaction time, carrier gas flow rate, pressure, and substrate position are kept the same.

Characterization

The SEM images are obtained on a Nova 230 at 10–15 kV, 0.6 pA–100 nA. When preparing SEM samples, the samples are coated with platinum to avoid charging effects during observation. TEM images, SAED patterns, and EDS spectra are obtained on a JEOL JEM 2100F operated at 200 kV. The nanostructures are placed on a carbon-coated copper grid for TEM analysis using a nano-manipulator. The cross-sectional TEM images are obtained on a JEOL JEM-ARM200F. For cross-sectional analysis, a NW transferred to a SiO_2 substrate is sliced and thinned by focused ion beam (FIB) and then supported on a TEM grid. The XRD patterns of the specimens are recorded on a RIGAKU Ultima IV diffractometer with filtered Cu Kα radiation.

Device fabrication

A single $Ag_2Se_{0.5}Te_{0.5}$ NW synthesized by the CVT method is transferred using a nano-manipulator onto a SiO_2/Si substrate with pre-patterned Ti/Au pads. The substrate is coated with poly(methyl methacrylate) (PMMA) (950 PMMA C4) and then baked at 180 °C for 2 min. E-beam lithography is performed using a field-emission SEM and ELPHY Quantum program. The selected areas around the single NW are exposed to the e-beam and then developed with methyl isobutyl ketone (MIBK) and isopropyl alcohol (IPA) solution. Ti/Au metal elec-

trodes are deposited by using an AC-sputter, and the lift-off process is carried out.

Measurements of electron transport properties

The fabricated NW devices are placed in a measurement mount, with electrical connections made with Au wire bonds. Transport measurements are carried out using a physical property measurement system from Quantum Design. The lowest temperature for the measurement is 2 K and the magnetic field is applied from −9 T to +9 T. For the angle-dependent electrical transport measurement, the sample is mounted on a rotating probe.

Crystal structure, band structure, and topological index calculations

An enthalpy minimization at zero pressure procedure is used to calculate lattice parameters and atomic positions in the unit cell. All calculations are performed using first-principles methods based on density functional theory as implemented in the Vienna *ab initio* simulation package (VASP).[50] The exchange–correlation energy functional is treated with the generalized gradient approximation by Perdew, Burke, and Ernzerhof.[51] A hybrid functional based on a screened Coulomb potential (HSE06) is also used.[52] Using a *k*-point mesh with a grid spacing of 0.2 Å^{-1}, we repeat the iterative calculation until all forces and stress tensors are less than 0.01 eV Å^{-1} and 1.5 kbar, respectively. We use the projector augmented wave pseudopotentials provided by VASP[53] and select 500 eV as the energy cut-off for the plane-wave basis set. An open-source software package WannierTools is used for the Wilson loop calculations.[38] The disentanglement procedure is tested on the extended 240 states and 40 states that cover the band inversion region. Within the inner energy window (4 eV) the agreement is virtually perfect. For the surface calculations, a 20-unit tight-binding supercell is constructed using maximally localized Wannier functions. The s orbitals of the Ag atoms and p orbitals of the Se and Te atoms are chosen as the projection centers. The number of Wannier functions and the number of bands are set to 40 and 240, respectively.

Conflicts of interest

There are no conflicts to declare.

Acknowledgements

References

1 M. Z. Hasan and C. L. Kane, *Rev. Mod. Phys.*, 2010, **82**, 3045–3067.

2 J. E. Moore, *Nature*, 2010, **464**, 194–198.

3 B. Q. Lv, H. M. Weng, B. B. Fu, X. P. Wang, H. Miao, J. Ma, P. Richard, X. C. Huang, L. X. Zhao, G. F. Chen, Z. Fang, X. Dai, T. Qian and H. Ding, *Phys. Rev. X*, 2015, **5**, 031013.

4 L. X. Yang, Z. K. Liu, Y. Sun, H. Peng, H. F. Yang, T. Zhang, B. Zhou, Y. Zhang, Y. F. Guo, M. Rahn, D. Prabhakaran, Z. Hussain, S. K. Mo, C. Felser, B. Yan and Y. L. Chen, *Nat. Phys.*, 2015, **11**, 728.

5 S. Y. Xu, I. Belopolski, N. Alidoust, M. Neupane, G. Bian, C. Zhang, R. Sankar, G. Chang, Z. Yuan, C. C. Lee, S. M. Huang, H. Zheng, J. Ma, D. S. Sanchez, B. K. Wang, A. Bansil, F. Chou, P. P. Shibayev, H. Lin, S. Jia and M. Z. Hasan, *Science*, 2015, **349**, 613–617.

6 Z. K. Liu, B. Zhou, Y. Zhang, Z. J. Wang, H. M. Weng, D. Prabhakaran, S. K. Mo, Z. X. Shen, Z. Fang, X. Dai, Z. Hussain and Y. L. Chen, *Science*, 2014, **343**, 864–867.

7 Z. Wang, Y. Sun, X. Q. Chen, C. Franchini, G. Xu, H. Weng, X. Dai and Z. Fang, *Phys. Rev. B: Condens. Matter Mater. Phys.*, 2012, **85**, 195320.

8 Z. Wang, H. Weng, Q. Wu, X. Dai and Z. Fang, *Phys. Rev. B: Condens. Matter Mater. Phys.*, 2013, **88**, 125427.

9 X. L. Qi and S. C. Zhang, *Rev. Mod. Phys.*, 2011, **83**, 1057.

10 S. Jia, S. Y. Xu and M. Z. Hasan, *Nat. Mater.*, 2016, **15**, 1140–1144.

11 S. Y. Xu, C. Liu, S. K. Kushwaha, R. Sankar, J. W. Krizan, I. Belopolski, M. Neupane, G. Bian, N. Alidoust, T. R. Chang, H. T. Jeng, C. Y. Huang, W. F. Tsai, H. Lin, P. P. Shibayev, F. C. Chou, R. J. Cava and M. Z. Hasan, *Science*, 2015, **347**, 294–298.

12 F. Xiu, L. He, Y. Wang, L. Cheng, L. Te Chang, M. Lang, G. Huang, X. Kou, Y. Zhou, X. Jiang, Z. Chen, J. Zou, A. Shailos and K. L. Wang, *Nat. Nanotechnol.*, 2011, **6**, 216–221.

13 J. G. Checkelsky, Y. S. Hor, R. J. Cava and N. P. Ong, *Phys. Rev. Lett.*, 2011, **106**, 196801.

14 S. Cho, B. Dellabetta, R. Zhong, J. Schneeloch, T. Liu, G. Gu, M. J. Gilbert and N. Mason, *Nat. Commun.*, 2015, **6**, 7634.

15 S. S. Hong, J. J. Cha, D. Kong and Y. Cui, *Nat. Commun.*, 2012, **3**, 757.

16 Z. Ren, A. A. Taskin, S. Sasaki, K. Segawa and Y. Ando, *Phys. Rev. B: Condens. Matter Mater. Phys.*, 2012, **85**, 155301.

17 L. L. Wang and D. D. Johnson, *Phys. Rev. B: Condens. Matter Mater. Phys.*, 2011, **83**, 241309.

18 L. Bao, L. He, N. Meyer, X. Kou, P. Zhang, Z.-G. Chen, A. V. Fedorov, J. Zou, T. M. Riedemann, T. A. Lograsso, K. L. Wang, G. Tuttle and F. Xiu, *Sci. Rep.*, 2012, **2**, 726.

19 D. O. Scanlon, P. D. C. King, R. P. Singh, A. De La Torre, S. M. K. Walker, G. Balakrishnan, F. Baumberger and C. R. A. Catlow, *Adv. Mater.*, 2012, **24**, 2154–2158.

20 T. Arakane, T. Sato, S. Souma, K. Kosaka, K. Nakayama, M. Komatsu, T. Takahashi, Z. Ren, K. Segawa and Y. Ando, *Nat. Commun.*, 2012, **3**, 636.

21 D. Kong, Y. Chen, J. J. Cha, Q. Zhang, J. G. Analytis, K. Lai, Z. Liu, S. S. Hong, K. J. Koski, S. K. Mo, Z. Hussain, I. R. Fisher, Z. X. Shen and Y. Cui, *Nat. Nanotechnol.*, 2011, **6**, 705–709.

22 Z. K. Liu, L. X. Yang, Y. Sun, T. Zhang, H. Peng, H. F. Yang, C. Chen, Y. Zhang, Y. F. Guo, D. Prabhakaran, M. Schmidt, Z. Hussain, S. K. Mo, C. Felser, B. Yan and Y. L. Chen, *Nat. Mater.*, 2016, **15**, 27.

23 S. Chadov, X. Qi, J. Kübler, G. H. Fecher, C. Felser and S. C. Zhang, *Nat. Mater.*, 2010, **9**, 541.

24 C. Shekhar, A. K. Nayak, S. Singh, N. Kumar, S.-C. Wu, Y. Zhang, A. C. Komarek, E. Kampert, Y. Skourski, J. Wosnitza, W. Schnelle, A. McCollam, U. Zeitler, J. Kubler, S. S. P. Parkin, B. Yan and C. Felser, 2016, arXiv:1604.01641.

25 Z. Zhao, S. Wang, A. R. Oganov, P. Chen, Z. Liu and W. L. Mao, *Phys. Rev. B: Condens. Matter Mater. Phys.*, 2014, **89**, 180102.

26 J. Kim, A. Hwang, S. H. Lee, S. H. Jhi, S. Lee, Y. C. Park, S. I. Kim, H. S. Kim, Y. J. Doh, J. Kim and B. Kim, *ACS Nano*, 2016, **10**, 3936–3943.

27 C.-L. Zhang, F. Schindler, H. Liu, T.-R. Chang, S.-Y. Xu, G. Chang, W. Hua, H. Jiang, Z. Yuan, J. Sun, H.-T. Jeng, H.-Z. Lu, H. Lin, M. Z. Hasan, X. C. Xie, T. Neupert and S. Jia, *Phys. Rev. B*, 2017, **96**, 165148.

28 W. Zhang, R. Yu, W. Feng, Y. Yao, H. Weng, X. Dai and Z. Fang, *Phys. Rev. Lett.*, 2011, **106**, 156808.

29 S. Lee, J. In, Y. Yoo, Y. Jo, Y. C. Park, H. Kim, H. C. Koo, J. Kim, B. Kim and K. L. Wang, *Nano Lett.*, 2012, **12**, 4194–4199.

30 A. Sulaev, P. Ren, B. Xia, Q. H. Lin, T. Yu, C. Qiu, S. Y. Zhang, M. Y. Han, Z. P. Li, W. G. Zhu, Q. Wu, Y. P. Feng, L. Shen, S. Q. Shen and L. Wang, *AIP Adv.*, 2013, **3**, 032123.

31 A. Sulaev, W. Zhu, K. Teo and L. Wang, *Sci. Rep.*, 2015, **5**, 1–7.

32 F. Virot, R. Hayn, M. Richter and J. Van Den Brink, *Phys. Rev. Lett.*, 2011, **106**, 236806.

33 V. E. Sacksteder, S. Kettemann, Q. Wu, X. Dai and Z. Fang, *Phys. Rev. B: Condens. Matter Mater. Phys.*, 2012, **85**, 205303.

34 F. Drymiotis, T. W. Day, D. R. Brown, N. A. Heinz and G. J. Snyder, *Appl. Phys. Lett.*, 2013, **103**, 143906.

35 T. W. Day, PhD thesis, California Institute of Technology, 2015.

36 J. H. Yun, M.-H. Lee, J. N. Kim, J. H. Shim and J.-S. Rhyee, *J. Appl. Phys.*, 2016, **119**, 165101.

37 I.-H. Lee, Y. J. Oh, S. Kim, J. Lee and K. J. Chang, *Comput. Phys. Commun.*, 2016, **203**, 110–121.

38 Q. S. Wu, S. N. Zhang, H. F. Song, M. Troyer and A. A. Soluyanov, *Comput. Phys. Commun.*, 2018, **224**, 405–416.

39 S. S. Hong, Y. Zhang, J. J. Cha, X. L. Qi and Y. Cui, *Nano Lett.*, 2014, **14**, 2815–2821.

40 H. Peng, K. Lai, D. Kong, S. Meister, Y. Chen, X. L. Qi, S. C. Zhang, Z. X. Shen and Y. Cui, *Nat. Mater.*, 2010, **9**, 225–229.

41 T. Ihn, *Nat. Mater.*, 2010, **9**, 187–188.

42 J. H. Bardarson, P. W. Brouwer and J. E. Moore, *Phys. Rev. Lett.*, 2010, **105**, 156803.

43 Y. Zhang and A. Vishwanath, *Phys. Rev. Lett.*, 2010, **105**, 206601.

44 R. Du, H. C. Hsu, A. C. Balram, Y. Yin, S. Dong, W. Dai, W. Zhao, D. Kim, S. Y. Yu, J. Wang, X. Li, S. E. Mohney, S. Tadigadapa, N. Samarth, M. H. W. Chan, J. K. Jain, C. X. Liu and Q. Li, *Phys. Rev. B*, 2016, **93**, 195402.

45 L. A. Jauregui, M. T. Pettes, L. P. Rokhinson, L. Shi and Y. P. Chen, *Nat. Nanotechnol.*, 2016, **11**, 345–351.

46 W. Ning, H. Du, F. Kong, J. Yang, Y. Han, M. Tian and Y. Zhang, *Sci. Rep.*, 2013, **3**, 1564.

47 J. J. Cha, M. Claassen, D. Kong, S. S. Hong, K. J. Koski, X. L. Qi and Y. Cui, *Nano Lett.*, 2012, **12**, 4355–4359.

48 K. S. Cho, T. Y. Huang, C. P. Huang, Y. H. Chiu, C. T. Liang, Y. F. Chen and I. Lo, *J. Appl. Phys.*, 2004, **96**, 7370–7373.

49 L. Barreto, L. Kühnemund, F. Edler, C. Tegenkamp, J. Mi, M. Bremholm, B. B. Iversen, C. Frydendahl, M. Bianchi and P. Hofmann, *Nano Lett.*, 2014, **14**, 3755–3760.

50 G. Kresse and J. Furthmüller, *Phys. Rev. B: Condens. Matter Mater. Phys.*, 1996, **54**, 11169.

51 J. P. Perdew, K. Burke and M. Ernzerhof, *Phys. Rev. Lett.*, 1996, **77**, 3865.

52 J. Heyd, G. E. Scuseria and M. Ernzerhof, *J. Chem. Phys.*, 2006, **124**, 219906.

53 D. Joubert, *Phys. Rev. B: Condens. Matter Mater. Phys.*, 1999, **59**, 1758.